Nanoscale

PAPER

Cite this: *Nanoscale*, 2015, **7**, 11093

Electrospun porous carbon nanofiber@MoS_2 core/sheath fiber membranes as highly flexible and binder-free anodes for lithium-ion batteries†

Yue-E Miao, Yunpeng Huang, Longsheng Zhang, Wei Fan, Feili Lai and Tianxi Liu*

Received 27th April 2015,
Accepted 17th May 2015

DOI: 10.1039/c5nr02711j

www.rsc.org/nanoscale

Self-standing membranes of porous carbon nanofiber (PCNF)@MoS_2 core/sheath fibers have been facilely obtained through a combination of electrospinning, high-temperature carbonization and the solvothermal reaction. PCNF fibers with porous channels are used as building blocks for the construction of hierarchical PCNF@MoS_2 composites where thin MoS_2 nanosheets are uniformly distributed on the PCNF surface. Thus, a three-dimensional open structure is formed, which provides a highly conductive pathway for rapid charge-transfer reactions, as well as greatly improving the surface active sites of MoS_2 for fast lithiation/delithiation of Li^+ ions. The highly flexible PCNF@MoS_2 composite membrane electrode exhibits synergistically improved electrochemical performance with a high specific capacity of 954 mA h g^{-1} upon the initial discharge, a high rate capability of 475 mA h g^{-1} even at a high current density of 1 A g^{-1}, and good cycling stability with almost 100% retention after 50 cycles, indicating its potential application as a binder-free anode for high-performance lithium-ion batteries.

1 Introduction

With severe stress from the energy crisis and global environmental concerns, lithium-ion batteries (LIBs) have attracted extensive attention as power sources for electric vehicles due to their high energy density, low gravimetric density, long cycle life, and flexible design. Therefore, new electrode materials with high capacity and excellent stability, such as two-dimensional (2D) transition-metal dichalcogenides MX_2 (M = Ti, Nb, Mo, Ta; X = S, Se, Te), have been considered as promising anode materials for LIBs. As a typical 2D transition-metal sulfide, MoS_2 shows an analogous layered structure of graphene in which molybdenum atoms are sandwiched between two layers of sulfur atoms, being one of the most stable and versatile members of the layered material family.[1–3] Moreover, the weak van der Waals interactions between MoS_2 layers give rise to wide interlayer spaces that reduce the barriers to Li^+ ion mobility and facilely allow the initial intercalation of Li^+ ions to form Li_2S, which is a prerequisite to fast lithiation/delithiation processes of Li_2S during the following charge/discharge cycles and thus results in high specific capacity.[4–6] Hence, various multilayered MoS_2 nanostructures, such as nanoflakes, nanoflowers, nanowires and nanotubes have been intensively explored as cathodes and anodes for LIBs.[7–10] However, these MoS_2 nanostructures suffer from severe restacking and condensation during charge/discharge processes due to the high surface energy, interlayer van der Waals attraction and poor conductivity, which results in drastically reduced accessibility of electrolytes and fast capacity fading in practical applications.[11,12]

To enhance the electrochemical performance of MoS_2, a feasible strategy is to construct hybrid nanostructures of MoS_2 with a highly conductive and flexible matrix, such as carbon spheres, carbon nanotubes, graphene and carbon cloth.[13–20] Hierarchical MoS_2 shells supported on carbon spheres have been synthesized through a one-step hydrothermal method, manifesting high specific capacity, enhanced cycling stability and good rate capability.[21] Cao *et al.* reported the preparation of MoS_2-coated three-dimensional graphene network composites *via* a facile chemical vapor deposition method.[22] The interconnected graphene sheets serve as the template for loading MoS_2 as well as providing good electrical contact between the current collector and deposited MoS_2, thus achieving a highly reversible capacity of 877 mA h g^{-1} at 100 mA g^{-1} and excellent high-current-density performance with a 10^{th}-cycle capacity of 466 mA h g^{-1} at a high current density of 4 A g^{-1}. A synergistic effect was also achieved with MoS_2 decorated biomass-derived carbon nanofibers,[23] where a persistent oxidation from Mo (or MoS_2) to MoS_3 took place in the repeated charge processes, leading to an ascending capacity upon

State Key Laboratory of Molecular Engineering of Polymers, Department of Macromolecular Science, Fudan University, Shanghai 200433, PR China. E-mail: txliu@fudan.edu.cn; Fax: +86-21-65640293; Tel: +86-21-55664197

†Electronic supplementary information (ESI) available. See DOI: 10.1039/c5nr02711j

cycling for high-energy lithium-ion batteries. Whereas, most of the above powdery materials need to be mixed with conductive additives and polymer binders to form film electrodes, which can hardly be flexible enough to meet tough environmental situations. Furthermore, the cumbersome process with introduction of excess binding agents may severely block the diffusion channels of ion transportation and largely affect the electrochemical performance. Thus, superior binder-free electrode materials with high flexibility and foldability are urgently needed for the development of new-generation lithium-ion batteries.

Rapid progress in portable electronics has also promoted increasing demand for high-performance energy-storage systems which are ultrathin, light weight, flexible, and even foldable or wearable.[24–26] An ideal highly flexible and binder-free electrode should simultaneously satisfy many critical features including high conductivity, structural durability and efficient ion transport, thus making it still a great challenge to design and fabricate high-performance flexible electrodes for LIBs.[27–29] For example, Chen *et al.* have developed additive-free electrode materials consisting of gel-like TiO_2-based nanotubes with controllable aspect ratios *via* a facile stirring hydrothermal method, which demonstrates ultrahigh rates and long lifetimes over 6000 charge/discharge cycles attributed to the high electronic/ionic conductivity and short lithium diffusion length.[30,31] Electrospinning is a promising and straightforward technique that produces free-standing nanofiber membranes with unique three-dimensional (3D) fiber networks, good structural stability and high flexibility, which can efficiently avoid the tedious preparation process of electrodes by using binders and conductive additives, as well as providing a shortened pathway for reduced internal resistance and easy access of electrolytes.[32–35] In particular, electrospun carbon nanofibers (CNFs) have been playing a leading role in LIBs due to their high surface area, controllable electronic conductivity and simplicity of preparation.[36–38] For instance, nitrogen-enriched porous carbon nanofiber networks (NPCNFs) have been successfully obtained by using low cost melamine and polyacrylonitrile as precursors *via* electrospinning, followed by carbonization and NH_3 treatments.[39] The NPCNFs exhibit well-developed microporous structure, inter-connected nanofibrous morphology with large specific surface area, and relatively high-level nitrogen doping efficiency for high-performance LIBs. Moreover, the electrospun carbon nanofiber-based composite membranes exhibit easily controllable thickness, high flexibility and good stability compared with other 3D framework (such as graphene film, network and aerogel)-templated nanocomposites, which effectively avoids the cumbersome process and remarkably simplifies the practical mass production of binder-free anodes for portable electronic applications.[40,41]

In this work, self-standing membranes of porous carbon nanofiber (PCNF)@MoS_2 core/sheath fibers have been facilely obtained through the combination of electrospinning and solvothermal reaction. Thin MoS_2 nanosheets are uniformly distributed on the surface of the PCNF core with porous channels to form a three-dimensional network which is favorable for rapid charge-transfer reactions and fast lithiation/delithiation of Li^+ ions. Thus, synergistically improved electrochemical performance is achieved with a high specific capacity of 954 mA h g^{-1} upon the initial discharge and a high rate capability of 475 mA h g^{-1} even at a high current density of 1 A g^{-1}. Moreover, the highly conductive PCNF core can effectively prevent the restacking and volume change of MoS_2 nanosheets during charge/discharge processes, which results in a good cycling stability with almost 100% reversible retention after 50 cycles, making the PCNF@MoS_2 composite membrane a promising binder-free anode for high-energy lithium-ion batteries.

2 Experimental section

2.1 Materials

Polyacrylonitrile (PAN) (M_w = 150 000 g mol^{-1}) was purchased from Sigma-Aldrich. Polystyrene (PS) (M_w = 280 000 g mol^{-1}) was obtained from Secco Co. Ltd, China. Ammonium tetrathiomolybdate ($(NH_4)_2MoS_4$) was purchased from J&K Chemical, with a purity of 99%. H_2SO_4 (95–98%), and *N*,*N*-dimethylformamide (DMF, ≥99.5%) were supplied by Shanghai Chemical Reagent Company. Electrolyte ($LiPF_6$ (1 M) in a mixture of ethylene carbonate (EC), ethyl methyl carbonate (EMC) and dimethyl carbonate (DMC) (1/1/1 in v/v/v)), lithium foils and Celgard-2400 were purchased from Shanxi Lizhiyuan Co. Ltd, China.

2.2 Preparation of electrospun PCNF@MoS_2 core/sheath fiber membranes

First, bicomponent PAN/PS nanofibers were produced through a facile single-nozzle electrospinning technique. Briefly, homogeneous solutions of PAN/PS in DMF were prepared with the solid content of PAN fixed at 10 wt% and sucked into a syringe with a needle having an inner diameter of 0.5 mm. The electrospinning process was carried out at an applied voltage of 15–20 kV with a feeding speed of 0.25 mL h^{-1} and a distance of 20 cm between the tip of the needle and the collector. The generated PAN/PS fibrous membranes were then pre-oxidized under 250 °C in an air atmosphere for 1 h at a heating rate of 1 °C min^{-1}, followed by heating up to 800 °C at a rate of 5 °C min^{-1} and carbonized for 2 h under a N_2 atmosphere. To investigate the pore-forming effect on the morphology and electrochemical properties, porous carbon nanofibers derived from specific PAN/PS weight ratios (w/w) of 90/10, 80/20, 70/30 were prepared and denoted as PCNF-10, PCNF-20 and PCNF-30, respectively. CNF fiber membranes obtained from the PAN/DMF solution without the introduction of PS were also prepared for comparison.

After that, PCNF@MoS_2 core/sheath fiber membranes with different loading amounts of MoS_2 were prepared by a one-step solvothermal reaction according to our previous method.[42] Briefly, the as-prepared PCNF-20 membranes were first treated in a bath of H_2SO_4 (98 wt%) for 10 min, and

thoroughly rinsed with deionized water. Then, they were solvothermally treated in a stainless steel autoclave containing 10 mL DMF solution of $(NH_4)_2MoS_4$ with certain amounts (*i.e.*, 5 mg, 10 mg, and 20 mg, respectively) at 200 °C for 10 h. After cooling to room temperature, the samples were rinsed with DMF and water several times and dried in a vacuum oven at 50 °C for 6 h. The PCNF@MoS_2 core/sheath fiber membranes thus obtained with increasing $(NH_4)_2MoS_4$ concentrations were labeled PCNF-20@MoS_2-5, PCNF-20@MoS_2-10, and PCNF-20@MoS_2-20 respectively. The whole preparation procedure of PCNF@MoS_2 core/sheath nanofiber membranes is schematically shown in Fig. 1.

2.3 Characterization

The morphology of the samples was investigated using a field emission scanning electron microscope (FESEM, Ultra 55, Zeiss) at an acceleration voltage of 5 kV. All samples were coated with a thin layer of gold prior to FESEM observations. Transmission electron microscopy (TEM) and high-resolution transmission electron microscopy (HRTEM) observations were performed under an acceleration voltage of 200 kV with a JEOL JEM 2100 TEM. Brunauer–Emmett–Teller (BET) surface area was measured using a Belsorp-max surface area detecting instrument by N_2 physisorption at 77 K. X-ray diffraction (XRD) experiments of the samples were conducted from 2θ = 5° to 80° on an X'Pert Pro X-ray diffractometer with CuKα radiation (λ = 0.1542 nm) under a voltage of 40 kV and a current of 40 mA. Thermogravimetric analysis (Pyris 1 TGA) was performed under an air flow from 100 to 700 °C at a heating rate of 20 °C min^{-1}. X-ray photoelectron spectroscopy (XPS) analyses were carried out using a RBD upgraded PHI-5000C ESCA system (Perkin Elmer) with Mg Kα radiation ($h\nu$ = 1253.6 eV) or Al Kα radiation ($h\nu$ = 1486.6 eV). All XPS spectra were corrected using C 1s line at 284.6 eV while background subtraction was accomplished using RBD AugerScan 3.21 software.

2.4 Electrochemical measurements

Electrochemical experiments were carried out with 2025 coin-type half-battery cells assembled in an argon-filled glovebox (M.Braun Inertgas Systems Co. Ltd, Shanghai). $LiPF_6$ (1 M) in a mixture of EC, EMC and DMC (1/1/1 in v/v/v) was used as the electrolyte while lithium foils served as the counter and reference electrodes, a Celgard-2400 membrane as the separator and the as prepared flexible PCNF@MoS_2 core/sheath fiber membranes directly as the anodes. Cyclic voltammetry (CV) curves were obtained in an electrochemical workstation (CHI 660B) in the potential range of 0.01–3.0 V *vs.* Li/Li^+ at a scan rate of 0.1 mV s^{-1}. Galvanostatic charge–discharge measurements and rate-performance tests under different current densities were carried out in a LAND (Wuhan Rambo Testing Equipment Co. Ltd, China) between 0.01 and 3.0 V. The electrochemical impedance spectroscopy (EIS) was measured in the frequency range of 10^5 to 10^{-2} Hz with an AC voltage amplitude of 5 mV. For comparison, a slurry of 80 wt% MoS_2 powder obtained under the same solvothermal reaction, 10 wt% carbon black and 10 wt% poly(vinylidene fluoride) in *N*-methyl-2-pyrrolidinone was also cast onto a copper foil and investigated as the anode electrode.

3 Results and discussion

Morphology and fiber diameters of porous carbon nanofiber membranes were investigated by FESEM as shown in Fig. 2. Small-diameter nanofibers with bead formation are observed from PCNF-10 (Fig. 2a), which can be attributed to the low viscosity of the precursor solution that reaches the "spray-spin transition" region.[43] By increasing the loading amount of PS, more uniformly distributed nanofibers with an average diameter of about 700 nm are obtained for PCNF-20 (Fig. 2b). Nevertheless, beaded fibers with larger diameter again appear after increasing the weight ratio of PAN/PS to 70/30 (w/w)

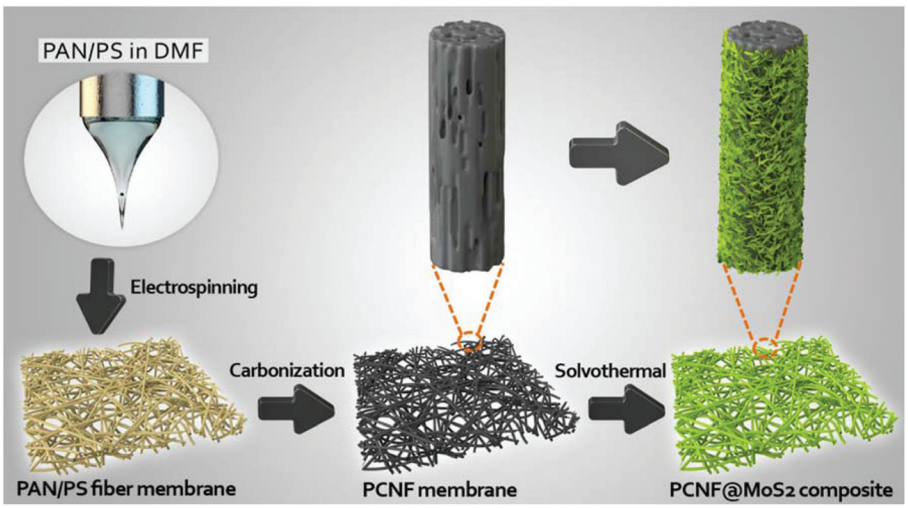

Fig. 1 Schematic for the preparation of electrospun PCNF@MoS_2 core/sheath fiber membranes.

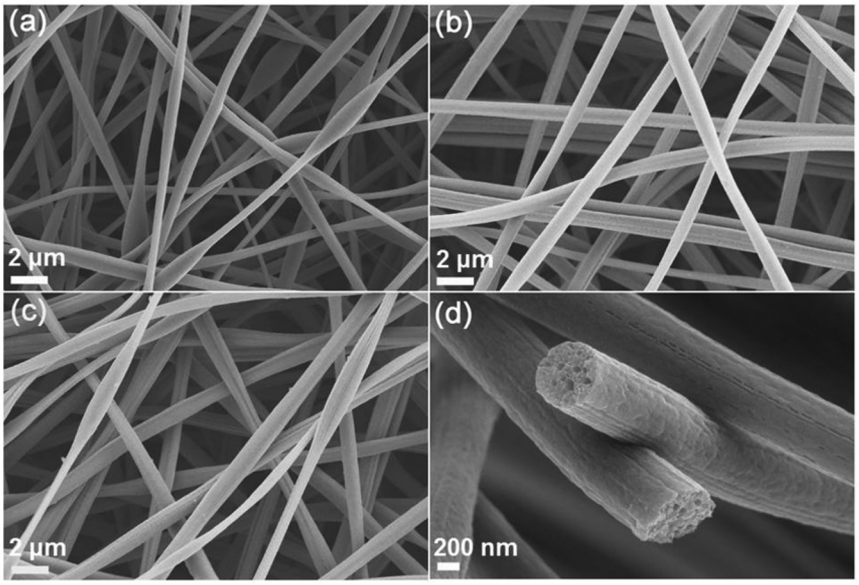

Fig. 2 FESEM images of electrospun PCNF-10 (a), PCNF-20 (b), PCNF-30 (c) fiber membranes; and the corresponding cross-section of PCNF-20 fiber membrane (d).

(Fig. 2c), which is due to the poor spinnability of the precursor solution caused by phase separation between PAN and PS.[44] It can be observed that the surface of PCNF-20 is smooth and almost free of defects such as beads, being able to provide a three-dimensional conductive template with good mechanical strength. Moreover, porous structures are obviously observed from the cross-sections of PCNF-20 nanofibers resulting from the decomposition of PS after carbonization (Fig. 2d), which are beneficial for efficient transport of ions and electrons. BET specific surface areas of PCNF-20 and CNF fiber membranes were further investigated by nitrogen adsorption/desorption isotherms (Fig. S1†). A type IV isotherm with a steep increase of nitrogen absorption at a high relative pressure (P/P_0 = 0.80–0.99) indicates that the main pore volume is contributed by large size pores. The PCNF-20 fiber membrane shows a greatly enhanced specific surface area (19.95 $m^2\ g^{-1}$) compared to that (2.49 $m^2\ g^{-1}$) of the CNF fiber membrane, suggesting that the introduction of a PS phase in PAN fibers could be an effective pore forming agent during the carbonization process. Therefore, a PCNF-20 fiber membrane is considered as a promising template for further construction of hierarchical nanostructures.

After *in situ* solvothermal treatment of PCNF-20 fiber membranes in DMF solution of $(NH_4)_2MoS_4$, MoS_2 nanoparticles are uniformly grown onto the surface of fibers to form a coaxial structure (Fig. 3a–c). Close observation of PCNF-20@MoS_2 core/sheath fibers (Fig. 3d) reveals that only nanoparticles with a diameter of about 200 nm can be obtained under a low dosage (5 mg) of $(NH_4)_2MoS_4$. By increasing $(NH_4)_2MoS_4$ concentration, thin curly MoS_2 nanosheets begin to form and closely lie on the surface of PCNF-20 fibers (Fig. 3e). Furthermore, MoS_2 nanosheets are found to grow perpendicularly on the surface of PCNF-20 fibers with dense accumulation when the dosage of $(NH_4)_2MoS_4$ is increased to 20 mg (Fig. 3f). Thus, hierarchical 3D nanostructures are facilely constructed through an effective combination of one-dimensional (1D) carbon nanofibers and 2D MoS_2 nanosheets, which can effectively prevent the aggregation of MoS_2 nanoparticles as well as offering an open structure beneficial for fast lithiation/delithiation during the charge/discharge processes. It is to be noticed that more large MoS_2 agglomerates are gradually formed with increasing initial concentration of $(NH_4)_2MoS_4$, which may be attributed to the rapid homogeneous nucleation of MoS_2 under high concentrations. In addition, no crack was observed upon bending of the PCNF-20@MoS_2-10 composite fiber membrane (as shown in the inset of Fig. 3b), indicating its high flexibility as a binder-free anode for LIBs, which can effectively avoid the cumbersome process for preparing MoS_2 nanoplatelet/carbon nanowire composite electrodes by using conductive additives and polymer binders as reported previously.[45]

The morphology of PCNF-20@MoS_2-10 composite fibers was further confirmed by TEM observations (Fig. 4). Porous channels are clearly observed from the PCNF core (red arrows in Fig. 4a), which is in good accordance with the FESEM observation, while the surface of PCNF is uniformly coated with many curly MoS_2 nanosheets. The HRTEM image (Fig. 4b) demonstrates that the MoS_2 nanosheet is accumulated by five to seven layers, with an interlayer spacing of approximately 0.65 nm, consistent with the *d*-spacing of (002) plane of hexagonal MoS_2.[21] This also accords with the XRD results of the as-prepared products (Fig. 5), where three distinct diffraction peaks at 2θ = 13.9°, 33.4°, and 58.9° represent the (002), (100), and (110) reflections of MoS_2, respectively. It must be empha-

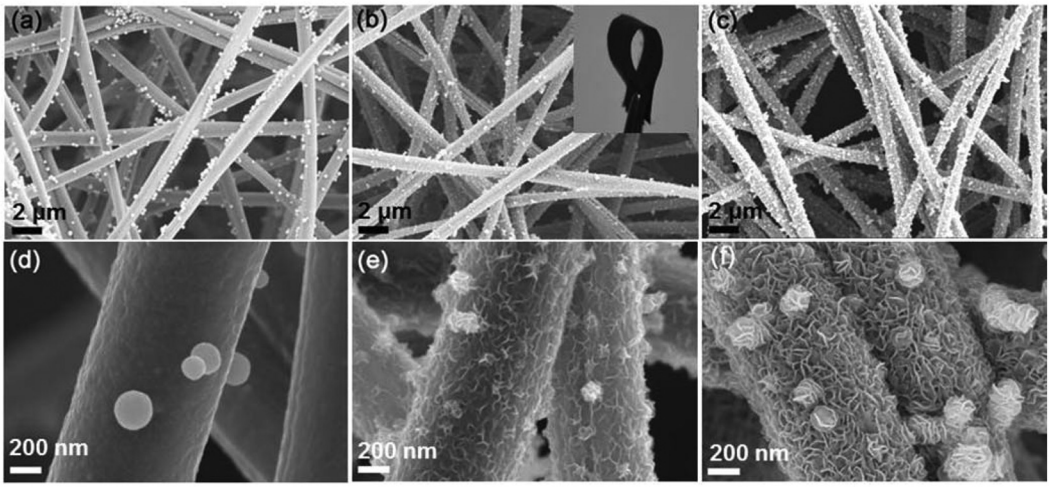

Fig. 3 Low and high magnification FESEM images of PCNF-20@MoS_2-5 (a, d), PCNF-20@MoS_2-10 (b, e), and PCNF-20@MoS_2-20 (c, f) composite fiber membranes. The inset of (b) is the corresponding digital photo of the highly flexible PCNF-20@MoS_2-10 composite membrane.

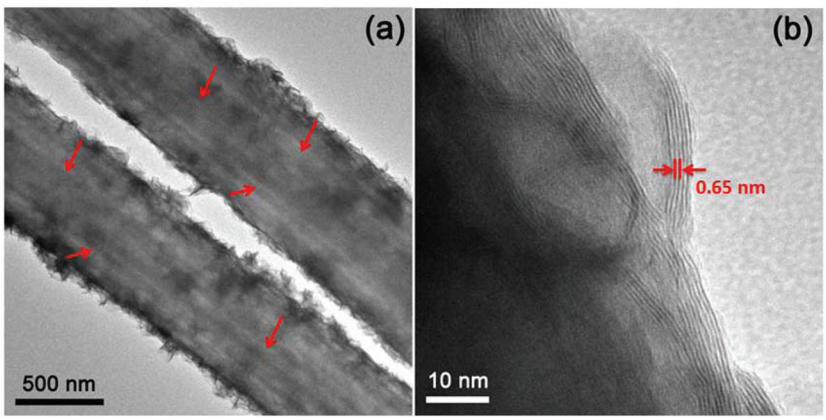

Fig. 4 TEM (a) and HRTEM (b) images of PCNF-20@MoS_2-10 composite fibers.

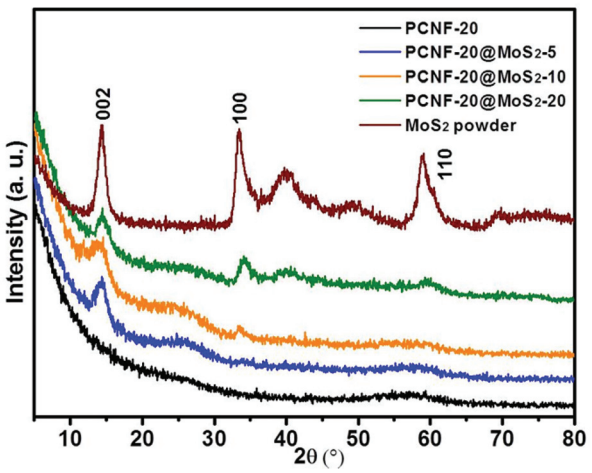

Fig. 5 XRD patterns of PCNF-20 fiber membranes, PCNF-20@MoS_2 composite fiber membranes, and MoS_2 powder.

sized that a shift of the (002) diffraction peak (from 16.7° to 13.9°) is obvious compared to the standard hexagonal 2H–MoS_2 structure (JPCDS 37-1492), revealing an expanded interlayer.[23] Thus, faster Li intercalation is expected upon the initial discharge process, which may lead to a higher electroactivity of MoS_2. The compositions and chemical states of the PCNF-20@MoS_2-10 composite fiber membrane were investigated by XPS spectra, with the survey scan indicating the coexistence of C, Mo, S, and O elements in the composite fiber membrane (Fig. 6a). High-resolution Mo 3d and S 2p spectra show characteristic peaks located at 232.6, 229.5, 163.5, and 162.2 eV corresponding to the binding energies of Mo $3d_{3/2}$, Mo $3d_{5/2}$, S $2p_{1/2}$, and S $2p_{3/2}$ components of MoS_2 respectively (Fig. 6b and c),[46] further indicating the successful acquisition of MoS_2 nanostructures on the PCNF fiber surface *via* the facile solvothermal reactions. The loading amounts of MoS_2 are calculated from the TGA curves (Fig. S2†), being 13.2%,

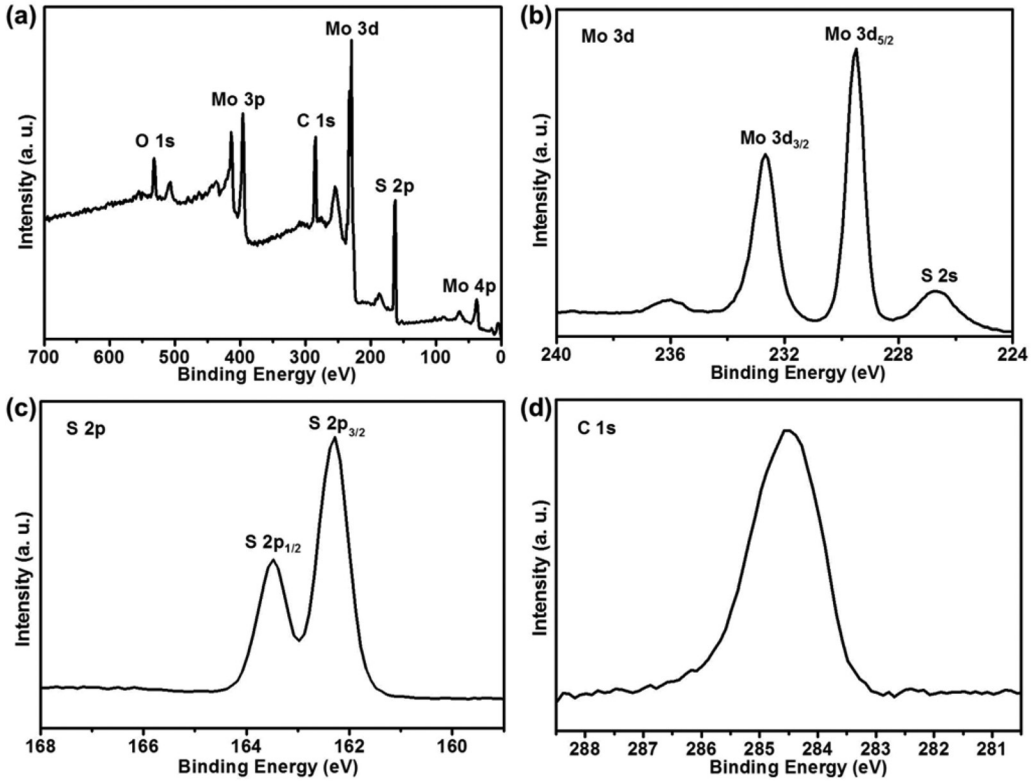

Fig. 6 XPS spectra of PCNF-20@MoS_2-10 composite fiber membranes: (a) the survey scan, (b) Mo 3d, (c) S 2p, (d) C 1s.

22.7%, and 37.2% for PCNF-20@MoS_2-5, PCNF-20@MoS_2-10, and PCNF-20@MoS_2-20, respectively.

To investigate the electrochemical performance, flexible PCNF and PCNF@MoS_2 fiber membranes were directly used as the anodes and assembled into Li half-cells. Fig. S3† shows the representative first-cycle discharge/charge voltage curves of PCNF nanofiber membranes, where the voltage plateau at 0.7 V can be ascribed to the formation of a solid electrolyte interface and electrolyte decomposition.[47,48] Discharge capacities of 618, 678, 680 mA h g^{-1} and reversible capacities of 301, 364, 345 mA h g^{-1} are observed for PCNF-10, PCNF-20 and PCNF-30 respectively, with initial Columbic efficiencies of 48.7%, 53.7%, and 50.7%. According to previous studies, the Columbic efficiency of carbon nanofibers can be improved by introducing closed pores that only allow access to Li^+.[49] Actually, a higher conductivity (1.45 S cm^{-1}) of PCNF-20 membranes has been achieved over that (0.50 S cm^{-1}) of CNF after being carbonized at 800 °C, further indicating that the porous structure of PCNF-20 fiber membranes obtained under an optimized content of a pore-forming agent of PS is beneficial for the improvement of electrical conductivity. High discharge capacities of 645, 954, 743 mA h g^{-1} and reversible capacities of 565, 730, 574 mA h g^{-1} are obtained for PCNF-20@MoS_2-5, PCNF-20@MoS_2-10, and PCNF-20@MoS_2-20, respectively (Fig. 7a). The much higher capacities and Columbic efficiencies of PCNF-20@MoS_2 composite fiber membranes than those of PCNF-20 fiber membranes are owing to the very good electrochemical activity (discharge capacity of 745 mA h g^{-1} and reversible capacity of 650 mA h g^{-1}) of MoS_2, which can effectively diminish the unfavorable contact between PCNF and the electrolyte, and thus help to prohibit the side reactions of PCNFs. According to a previous report,[50] normalized reversible capacities to the mass of MoS_2 are calculated to be 1955, 1976, and 929 mA h g^{-1} for PCNF-20@MoS_2-5, PCNF-20@MoS_2-10, and PCNF-20@MoS_2-20, respectively, much higher than that reported by encapsulating MoS_2 nanoflakes in carbon nanofibers (1133 mA h g^{-1}).[51] This can be ascribed to the more uniform distribution of 2D MoS_2 nanosheets on the 1D PCNF nanofiber surface instead of forming aggregations, which can effectively build up a hierarchical 3D nanostructure and provide an open structure facilitating fast lithiation/delithiation during the charge–discharge processes. Furthermore, it also gives a suitable explanation for the best electrochemical performance of the PCNF-20@MoS_2-10 composite membrane, in which MoS_2 nanosheets exhibit much more uniform distribution with less aggregations and better interfacial overlaps with the conductive PCNF template as shown in Fig. 3b and e.

In particular, two plateaus appear at approximately 1.1 V and 0.6 V in the first discharge process of PCNF-20@MoS_2 composite membranes and MoS_2 powder (Fig. 7a), which correspond to the insertion of Li^+ ions into the interlayer space of MoS_2 and further decomposition into Li_2S and Mo nanoparticles, respectively. To better reveal the electrochemistry

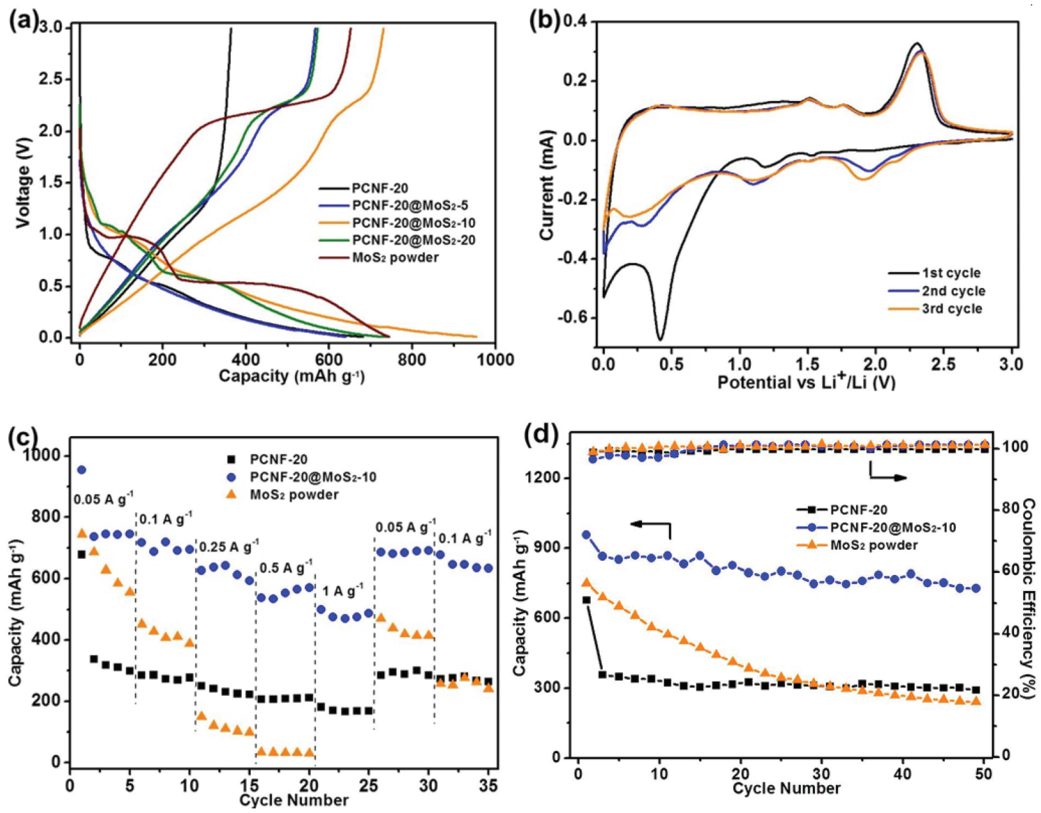

Fig. 7 (a) Initial charge/discharge curves of PCNF-20 fiber membranes, PCNF-20@MoS_2 composite fiber membranes, and MoS_2 powder at a current density of 0.05 A g^{-1}; (b) CV curves of PCNF-20@MoS_2-10 composite fiber membranes at the first three cycles at a scan rate of 0.1 mV s^{-1} between 0.01 V and 3 V; (c) rate behavior of PCNF-20 fiber membranes, PCNF-20@MoS_2 composite fiber membranes, and MoS_2 powder at various current densities; (d) cycling performance of PCNF-20 fiber membranes, PCNF-20@ MoS_2-10 composite fiber membranes, and MoS_2 powder at a current rate of 0.05 A g^{-1}.

during the cell testing process, CV curves of PCNF-20@MoS_2-10 composite membranes were collected in the potential window of 0.01–3.0 V at a scan rate of 0.1 mV s^{-1} (Fig. 7b). In the first cathodic process, two reduction peaks at approximately 1.2 V and 0.4 V are in good accordance with the first discharge process, representing Li intercalation into layered MoS_2 and conversion into Mo and Li_2S based on the following reactions:[52]

$$MoS_2 + xLi^+ + xe^- = Li_xMoS_2 \ (x = 3\text{–}4) \quad (1)$$

$$Li_xMoS_2 + 4Li^+ + 4e^- = 2Li_2S + Mo/Li_y \quad (2)$$

During the anodic scanning, three oxidation peaks appear with two small peaks at approximately 1.5 V and 1.8 V, respectively, corresponding to the stepped oxidations from Mo to Mo^{4+} and Mo^{6+}, while the oxidation peak at 2.3 V is derived from the oxidation of Li_2S to sulfur. In the subsequent cycles, two reduction peaks at 1.5 V and 1.1 V are attributed to the stepped reductions/oxidations between Mo^{6+} and Mo, while 1.9 V can be denoted as the sulfide redox reaction.

The rate capabilities were investigated by applying various current densities to the cells (Fig. 7c). The discharge capacity delivered by MoS_2 powder is only 28 mA h g^{-1} at a current density of 0.5 A g^{-1}, which clearly shows the rapid capacity fading of MoS_2 even at low discharge currents. In contrast, a PCNF-20@MoS_2-10 composite membrane exhibits a high discharge capacity of 1532 mA h g^{-1} (normalized to the mass of MoS_2) even at a high rate of 1 A g^{-1}, much higher than those (*e.g.*, 986 mA h g^{-1}, 250–350 mA h g^{-1}) previously reported for MoS_2 nanoflakes encapsulated in carbon nanofibers.[45,46] Moreover, the reversible capacity is restored to 690 mA h g^{-1} when the current rate is changed back to 0.05 A g^{-1}, approaching its initial capacity. Rate behaviors of different PCNF-20@MoS_2 composite membranes (Fig. S4†) further indicate that PCNF-20@MoS_2-10 composite fiber membranes exhibit higher discharge capacities over those of PCNF-20@MoS_2-5 and PCNF-20@MoS_2-20 composite fiber membranes under various current densities. The remarkably high rate capability of PCNF-20@MoS_2-10 composite membranes is due to the synergistic interactions between 1D PCNF nanofibers and 2D MoS_2 nanosheets, where the highly conductive PCNF nanofibers act both as the conductive support as well as the Li storage matrix to provide sufficient electrons for fast lithiation/delithiation of the MoS_2 sheath, thus resulting

in significantly improved electrochemical lithium storage performance of the PCNF-20@MoS_2-10 composite membrane under high current densities. Fig. 7d shows the cycling performance of PCNF-20 fiber membranes, PCNF-20@MoS_2-10 composite fiber membranes, and MoS_2 powder at a current rate of 0.05 A g^{-1}. Severe continuous discharge capacity decay can be observed for MoS_2 powder from an initial value of 745 mA h g^{-1} to 240 mA h g^{-1} after 50 cycles, merely delivering a low capacity retention of 32%. Whereas, the PCNF-20@MoS_2-10 composite fiber membrane still retains a high discharge capacity of 736 mA h g^{-1} after 50 cycles. Despite an initial irreversible capacity loss with the Coulombic efficiency of 76.5% due to the formation of SEI layers and trapping of lithium in the lattice or defects of MoS_2 during the first cycle, the Coulombic efficiency remains at almost 100% in the subsequent cycles, thus leading to excellent cycling performance with a reversible retention of about 100% (from the second cycle). As shown in Fig. S5,† the charge/discharge curves at 25th and 50th cycles exhibit high Coulombic efficiencies of 97.1% and 98.2%, respectively, indicating excellent stability and cycling performance for PCNF-20@MoS_2-10 composite fiber membranes. XRD patterns (Fig. S6†) of PCNF-20@MoS_2-10 composite fiber membranes after the cycling test show that most peaks of MoS_2 disappear while a new peak corresponding to Li_2S appears, which is in good accordance with the above reaction mechanism.[52] FESEM images of PCNF-20@MoS_2-10 composite fiber membranes after the cycling test (Fig. S7†) show that the nanoparticles are still uniformly covered on the surface of PCNF nanofibers although MoS_2 nanosheets convert into a mixture of sulfur and Mo metals after the first cycle, further proving that the PCNF nanofiber template plays a leading role in stabilizing the disordered structure and preventing the severe volume expansion/contraction of MoS_2 nanosheets during the repetitive lithium storage/release processes. Therefore, the PCNF-20@MoS_2-10 composite fiber membrane exhibits superior cycle performance compared to MoS_2 powder, making it promising as a highly flexible and binder-free anode for long-life LIBs.

EIS was measured to investigate the electrochemical impedance of the cells as shown in Fig. 8. The Nyquist plots consist of two semicircles at high and medium frequencies, as well as a straight line at a constant inclining angle at low frequencies, respectively, corresponding to the resistance of the solid electrolyte interface, charge-transfer resistance at the electrolyte/electrode interface, and the solid state diffusion resistance of Li^+ in the electrode.[51] The electrode–electrolyte interfacial resistances (R_i) are 110 Ω, 128 Ω, and 160 Ω for PCNF-20 fiber membranes, PCNF-20@ MoS_2-10 composite fiber membranes and MoS_2 powder, respectively. The remarkably reduced R_i value of PCNF-20@MoS_2-10 composite fiber membranes compared with that of MoS_2 powder indicates the greatly reduced charge-transfer resistance at the electrode/electrolyte interface due to the distinct combination of MoS_2 with the conductive PCNF nanofiber networks, which efficiently promotes the penetration of electrolytes and migration of lithium ions for better battery performance.

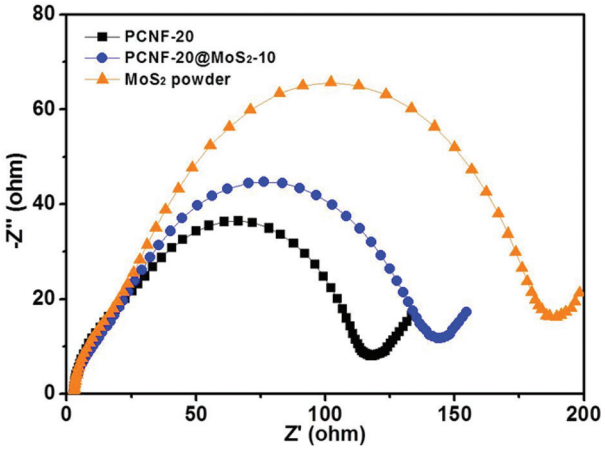

Fig. 8 Nyquist plots of PCNF-20 fiber membranes, PCNF-20@MoS_2-10 composite fiber membranes, and MoS_2 powder in the frequency range of 10^5 to 10^{-2} Hz with an AC voltage amplitude of 5 mV.

4 Conclusions

In summary, highly flexible PCNF@MoS_2 coaxial fiber membranes have been facilely obtained through a combination of electrospinning and the solvothermal reaction. The hierarchical 3D nanostructures *via* ingenious construction of 1D nanofibers and 2D nanosheets can effectively prevent the aggregation of MoS_2 nanoparticles as well as offering an open structure favorable for rapid charge-transfer reactions and fast lithiation/delithiation during the charge–discharge processes. The synergistic effects thus lead to remarkably improved electrochemical performance for a PCNF@MoS_2 composite fiber membrane with a high specific capacity of 954 mA h g^{-1} upon the initial discharge, a high rate capability of 475 mA h g^{-1} even at a high current density of 1 A g^{-1} and good cycling stability with almost 100% reversible retention after 50 cycles, making it a potential flexible and binder-free anode material for high-performance lithium-ion batteries.

Acknowledgements

The authors are grateful for financial support from the National Natural Science Foundation of China (51125011, 51373037, 51433001).

Notes and references

1 M. Chhowalla, H. S. Shin, G. Eda, L.-J. Li, K. P. Loh and H. Zhang, *Nat. Chem.*, 2013, **5**, 263–275.
2 H. S. S. Ramakrishna Matte, A. Gomathi, A. K. Manna, D. J. Late, R. Datta, S. K. Pati and C. N. R. Rao, *Angew. Chem., Int. Ed.*, 2010, **122**, 4153–4156.
3 C. N. R. Rao and A. Nag, *Eur. J. Inorg. Chem.*, 2010, **2010**, 4244–4250.

4 H. Hwang, H. Kim and J. Cho, *Nano Lett.*, 2011, **11**, 4826–4830.
5 A. V. Murugan, M. Quintin, M.-H. Delville, G. Campet, C. S. Gopinath and K. Vijayamohanan, *J. Power Sources*, 2006, **156**, 615–619.
6 Q. Wang and J. H. Li, *J. Phys. Chem. C*, 2007, **111**, 1675–1682.
7 S. J. Ding, D. Y. Zhang, J. S. Chen and X. W. Lou, *Nanoscale*, 2012, **4**, 95–98.
8 H. Li, W. Li, L. Ma, W. X. Chen and J. M. Wang, *J. Alloys Compd.*, 2009, **471**, 442–447.
9 C. Q. Feng, J. Ma, H. Li, R. Zeng, Z. P. Guo and H. K. Liu, *Mater. Res. Bull.*, 2009, **44**, 1811–1815.
10 S. F. Zhuo, Y. Xu, W. W. Zhao, J. Zhang and B. Zhang, *Angew. Chem., Int. Ed.*, 2013, **52**, 8602–8606.
11 J. Xiao, D. Choi, L. Cosimbescu, P. Koech, J. Liu and J. P. Lemmon, *Chem. Mater.*, 2010, **22**, 4522–4524.
12 G. D. Du, Z. P. Guo, S. Q. Wang, R. Zeng, Z. X. Chen and H. K. Liu, *Chem. Commun.*, 2010, **46**, 1106–1108.
13 S.-K. Park, S.-H. Yu, S. Woo, B. Quan, D.-C. Lee, M. K. Kim, Y.-E. Sung and Y. Piao, *Dalton Trans.*, 2013, **42**, 2399–2405.
14 S. J. Ding, J. S. Chen and X. W. Lou, *Chem. – Eur. J.*, 2011, **17**, 13142–13145.
15 K. Chang and W. X. Chen, *ACS Nano*, 2011, **5**, 4720–4728.
16 K. Bindumadhavan, S. K. Srivastava and S. Mahanty, *Chem. Commun.*, 2013, **49**, 1823–1825.
17 X. S. Zhou, L. J. Wan and Y. G. Guo, *Chem. Commun.*, 2013, **49**, 1838–1840.
18 H. L. Yu, C. Ma, B. H. Ge, Y. J. Chen, Z. Xu, C. L. Zhu, C. Y. Li, Q. Y. Ouyang, P. Gao, J. Q. Li, C. W. Sun, L. H. Qi, Y. M. Wang and F. H. Li, *Chem. – Eur. J.*, 2013, **19**, 5818–5823.
19 C. F. Zhang, Z. Y. Wang, Z. P. Guo and X. W. Lou, *ACS Appl. Mater. Interfaces*, 2012, **4**, 3765–3768.
20 C. Wang, W. Wan, Y. H. Huang, J. T. Chen, H. H. Zhou and X. X. Zhang, *Nanoscale*, 2014, **6**, 5351–5358.
21 L. Zhang and X. W. Lou, *Chem. – Eur. J.*, 2014, **20**, 5219–5223.
22 X. H. Cao, Y. M. Shi, W. H. Shi, X. H. Rui, Q. Y. Yan, J. Kong and H. Zhang, *Small*, 2013, **9**, 3433–3438.
23 F. Zhou, S. Xin, H.-W. Liang, L. T. Song and S. H. Yu, *Angew. Chem., Int. Ed.*, 2014, **53**, 11552–11556.
24 L. Li, Z. Wu, S. Yuan and X.-B. Zhang, *Energy Environ. Sci.*, 2014, **7**, 2101–2122.
25 H. Gwon, H.-S. Kim, K. U. Lee, D. H. Seo, Y. C. Park, Y.-S. Lee, B. T. Ahn and K. Kang, *Energy Environ. Sci.*, 2011, **4**, 1277–1283.
26 Z. Chen, D. Zhang, X. Wang, X. Jia, F. Wei, H. Li and Y. Lu, *Adv. Mater.*, 2012, **24**, 2030–2036.
27 N. Li, G. M. Zhou, F. Li, L. Wen and H.-M. Cheng, *Adv. Funct. Mater.*, 2013, **23**, 5429–5435.
28 X. Fang, M. Y. Ge, J. P. Rong and C. W. Zhou, *ACS Nano*, 2014, **8**, 4876–4882.
29 M. H. Chen, J. L. Liu, D. L. Chao, J. Wang, J. H. Yin, J. Y. Lin, H. Jin Fan and Z. Xiang Shen, *Nano Energy*, 2014, **9**, 364–372.
30 Y. X. Tang, Y. Y. Zhang, J. Y. Deng, J. Q. Wei, H. L. Tam, B. K. Chandran, Z. L. Dong, Z. Chen and X. D. Chen, *Adv. Mater.*, 2014, **26**, 6111–6118.
31 Y. X. Tang, Y. Y. Zhang, J. Y. Deng, D. P. Qi, W. R. Leow, J. Q. Wei, S. Y. Yin, Z. L. Dong, R. Yazami, Z. Chen and X. D. Chen, *Angew. Chem., Int. Ed.*, 2014, **53**, 13488–13492.
32 C. L. Zhang and S.-H. Yu, *Chem. Soc. Rev.*, 2014, **43**, 4423–4448.
33 Z. P. Zhou, X. F. Wu and H. Q. Hou, *RSC Adv.*, 2014, **4**, 23622–23629.
34 Y. E. Miao, G. N. Zhu, H. Q. Hou, Y. Y. Xia and T. X. Liu, *J. Power Sources*, 2013, **226**, 82–86.
35 Y. Y. Zhai, N. Wang, X. Mao, Y. Si, J. Y. Yu, S. S. Al-Deyab, M. El-Newehy and B. Ding, *J. Mater. Chem. A*, 2014, **2**, 14511–14518.
36 G. H. Zhang, J. Zhu, W. Zeng, S. C. Hou, F. L. Gong, F. Li, C. C. Li and H. G. Duan, *Nano Energy*, 2014, **9**, 61–70.
37 X. S. Zhou, Z. H. Dai, S. H. Liu, J. C. Bao and Y. G. Guo, *Adv. Mater.*, 2014, **26**, 3943–3949.
38 Z.-L. Xu, B. Zhang and J.-K. Kim, *Nano Energy*, 2014, **6**, 27–35.
39 D. Nan, Z.-H. Huang, R. T. Lv, L. Yang, J. G. Wang, W. C. Shen, Y. X. Lin, X. L. Yu, L. Ye, H. Y. Sun and F. Y. Kang, *J. Mater. Chem. A*, 2014, **2**, 19678–19684.
40 J. Lee, C. Jo, B. Park, W. Hwang, H. I. Lee, S. Yoon and J. Lee, *Nanoscale*, 2014, **6**, 10147–10155.
41 Y. H. Xu, Y. J. Zhu, F. D. Han, C. Luo and C. S. Wang, *Adv. Energy Mater.*, 2015, **5**, 1400753.
42 Y. P. Huang, Y. E. Miao, L. S. Zhang, W. W. Tjiu, J. S. Pan and T. X. Liu, *Nanoscale*, 2014, **6**, 10673–10679.
43 N. T. Xuyen, E. J. Ra, H. Z. Geng, K. K. Kim, K. H. An and Y. H. Lee, *J. Phys. Chem. B*, 2007, **111**, 11350–11353.
44 G. S. Park, J.-S. Lee, S. T. Kim, S. Park and J. Cho, *J. Power Sources*, 2013, **243**, 267–273.
45 C. B. Zhu, X. K. Mu, P. A. van Aken, Y. Yu and J. Maier, *Angew. Chem., Int. Ed.*, 2014, **53**, 2152–2156.
46 P. P. Wang, H. Y. Sun, Y. J. Ji, W. H. Li and X. Wang, *Adv. Mater.*, 2014, **26**, 964–969.
47 Y. M. Chen, X. Y. Li, K. Park, J. Song, J. H. Hong, L. M. Zhou, Y. W. Mai, H. T. Huang and J. B. Goodenough, *J. Am. Chem. Soc.*, 2013, **135**, 16280–16283.
48 L. G. Bulusheva, A. V. Okotrub, A. G. Kurenya, H. K. Zhang, H. J. Zhang, X. H. Chen and H. H. Song, *Carbon*, 2011, **49**, 4013–4023.
49 N. A. Kaskhedikar and J. Maier, *Adv. Mater.*, 2009, **21**, 2664–2680.
50 A. Ghosh, E. J. Ra, M. Jin, H. K. Jeong, T. H. Kim, C. Biswas and Y. H. Lee, *Adv. Funct. Mater.*, 2011, **21**, 2541–2547.
51 C. Y. Zhao, J. H. Kong, X. Y. Yao, X. S. Tang, Y. L. Dong, S. L. Phua and X. H. Lu, *ACS Appl. Mater. Interfaces*, 2014, **6**, 6392–6398.
52 J. Xiao, X. J. Wang, X. Q. Yang, S. D. Xun, G. Liu, P. K. Koech, J. Liu and J. P. Lemmon, *Adv. Funct. Mater.*, 2011, **21**, 2840–2846.